Mobile Integrated Profiler System (MIPS) Observations of Low-Level Convergent Boundaries during IHOP

HALDUN KARAN AND KEVIN KNUPP

University of Alabama in Huntsville, Huntsville, Alabama

(Manuscript received 6 October 2004, in final form 23 February 2005)

ABSTRACT

Characteristics of convergent boundary zones (CBZs) sampled by the Mobile Integrated Profiling System (MIPS) during the 2002 International H_2O Project (IHOP_2002) are presented. The MIPS sensors (915-MHz wind profiler, 12-channel microwave profiling radiometer, ceilometer, and surface instrumentation) provide very fine temporal kinematic and thermodynamic profiles of the atmospheric boundary layer and CBZ properties, including enhanced 915-MHz backscatter within the CBZ updraft (equivalent to the radar fine line), a general increase in integrated water vapor within the updrafts of the CBZ, an increase in the convective boundary layer (CBL) depth, and changes in ceilometer backscatter that are typically coincident with arrival of cooler, moister air (the case for density current CBZ).

Three contrasting CBZs are analyzed. Convective initiation was associated with a slow-moving dryline as it passed over the MIPS on 19 June. Updrafts up to 6 m s^{-1} were measured, and the CBL attained its greatest depth within the CBZ. The CBZ in the other two cases were quite similar to density currents. The retrograding dryline of 18 June produced an enhancement in preexisting convection within 30 km of the MIPS. On 24 May, a shallow cold front, about 800 m deep, was sampled.

1. Introduction

During the International H_2O Project (IHOP; Weckwerth et al. 2004), the Mobile Integrated Profiling System (MIPS), other mobile ground-based platforms, and instrumented aircraft acquired comprehensive datasets on convergent boundary zones (CBZs), in support of convective initiation (CI) experiments. About 12 CI missions were conducted during the 7-week field phase. In this paper we describe microscale properties of CBZ using MIPS datasets for three contrasting boundaries, including a slowly moving dryline, a retrograding dryline, and a shallow cold front.

This research is part of a longer-term project entitled the Atmospheric Boundary Identification and Delineation Experiment (ABIDE). The main goal of ABIDE is to develop a comprehensive characterization of the kinematic, thermodynamic, and dynamic properties of CBZ for a wide spectrum of environmental types. Examples of CBZ include fronts, thunderstorm outflow boundaries, gust fronts, drylines, sea breezes, and gravity wave phenomena. These boundaries present a broad range of kinematic and thermodynamic properties, and spatial/temporal scales. A second ABIDE objective is to conduct detailed, multisensor case studies (using the MIPS plus Doppler radar; e.g., Knupp and Karan 2005, manuscript submitted to *Mon. Wea. Rev.*) of significant CBZs, and CBZs that produce convective initiation.

Numerous investigations of CBZs have utilized Doppler radar and surface mesonet platforms in various field studies, including the Convective Initiation Downburst Experiment in Colorado (CINDE; Wilson and Schreiber 1986; Wilson et al. 1994), the Cooperative Oklahoma Profiler Studies (COPS-91) and Verification of the Origins of Rotation in Tornadoes Experiment (VORTEX; Ziegler and Rasmussen 1998; Weiss and Bluestein 2002; Hane et al. 2002; Rasmussen et al. 2000) programs in Oklahoma, and the Convection and Precipitation Electrification Experiment (CaPE; Atkins et al. 1995; Wilson and Megenhardt 1997; Kingsmill and Crook 2003) in Florida. Multiple-Doppler radar analyses portray 3D structures of these features, but they lack high accuracy and vertical resolution in retrieved *W* fields. The reader is referred to

Corresponding author address: Haldun Karan, Dept. of Atmospheric Science, University of Alabama in Huntsville, NSSTC, 320 Sparkman Drive, Huntsville, AL 35805.
E-mail: karan@nsstc.uah.edu

TABLE 1. MIPS sensors and their measurement characteristics.

Instrument	Quantities measured or calculated	Measurement height	Vertical resolution	Temporal resolution	Dwell time
915-MHz profiler	Signal-to-noise ratio (C_n^2), vertical velocity, spectral width (SW), horizontal wind (W), Doppler spectra	0.12 to 4 km	105 m	60 s	30 s
Ceilometer	Two-way backscatter, cloud base	30 m to 7.6 km	30 m	15 s	15 s
MPR	Temperature, mixing ratio, liquid water, integrated water vapor, integrated cloud water	Surface to 10 km	Variable, scales with height 100 m from surface to 1 km, then 250 m up to 10 km	14 min	N/A
Doppler sodar	SNR (C_T^2), W, SW, horizontal wind	50 to 100–400 m	25 m	20 s	N/A
Surface	Temperature, relative humidity, pressure, wind, solar radiation	4 m	N/A	1 s	1 s

Weckwerth and Parsons (2006) for a more thorough review of CBZs and their role in convective initiation.

Direct observations of CBZ vertical structure have been limited to a few *vertically* pointing Doppler radar (Martner 1997; May 1999; Ralph et al. 1999; Neiman et al. 2001) and aircraft measurements (Ziegler and Hane 1993). While thermodynamic properties within CBZs have been probed with aircraft and surface instrumentation (Hane et al. 2002), accurate and continuous measurements over the entire CBZ depth and the adjacent atmospheric boundary layer have been limited. The MIPS provides a capability to simultaneously measure CBZ and atmospheric boundary layer (ABL) kinematics and thermodynamics from a fixed point. In particular, very accurate measurements of CBZ updraft profiles are acquired. Such measurements provide a quasi-two-dimensional representation of CBZ properties, with the assumption that the kinematic and thermodynamic fields are stationary during the period when the CBZ translates over the MIPS site.

In this paper we present analyses of MIPS measurements from three cases, two (a cold front on 24 May and a dryline on 19 June 2002) of which are considered in greater detail by other IHOP investigators (Geerts et al. 2006; Murphey et al. 2006; Wakimoto et al. 2006). A summary of MIPS measurements is presented in section 2. Sections 3–5 present measurements for three contrasting CBZs: a slow advancing dryline, a retrograding dryline, and a shallow cold front. A summary and conclusions follows in section 6.

2. Observational datasets and methodology

a. Observational platforms

The primary datasets used in this study were obtained by MIPS, which consisted of a 915-MHz boundary layer wind profiler (Radian LAP-3000), a 12-channel microwave profiling radiometer (MPR; Radiometrics TP/WVP-3000), a lidar ceilometer (Vaisala CT-25k), a Doppler sodar, and surface instrumentation. Table 1 presents more detailed specifications of each instrument. The MIPS is shown in Fig. 1 during one of the IHOP deployments (18 June) considered in this paper. This was a typical roadside operation in southwest Kansas, free of nearby ground clutter objects such as pivot irrigation systems, fences, and power lines. Because clutter panels were not used on the 915-MHz profiler, great care was taken during IHOP to search for clutter-free sites such as this in order to minimize ground clutter contamination in the lowest range gates.

The basic MIPS measurements are provided in Table 1. The suite of MIPS instruments provided continuous monitoring of ABL thermodynamic and kinematic

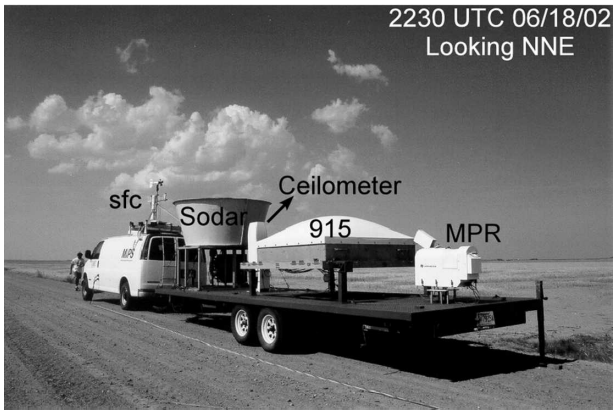

FIG. 1. MIPS deployment for a convective initiation experiment on 18 Jun 2002. The MIPS is facing north on a north–south gravel road. This was considered an ideal site far removed from clutter objects such as power lines, wire fences, pivot irrigation systems, and tall, active vegetation (e.g., corn).

properties, within a small mesoscale domain monitored by other facilities, including up to four mobile Doppler radars, mobile mesonet vehicles, and aircraft platforms. The 915-MHz profiler provided vertical motion to about 0.2 m s^{-1} accuracy (within large eddies and boundaries), horizontal wind to 1 m s^{-1} accuracy, and ABL properties inferred from signal-to-noise ratio (SNR) and large eddy turbulence as indicated by vertical motion measurements acquired every 60 s. The ceilometer measured relative aerosol loading across boundaries, as well as cloud-base height, at 15-s and 30-m temporal and vertical resolution, respectively.

The MPR directly measures atmospheric microwave emissions around the water vapor absorption band (22–31 GHz, five channels) and the O_2 absorption band (51–59 GHz, seven channels) that are converted to brightness temperatures (T_B). The MPR field of view is 2°–3° at 51–59 GHz and 5°–6° at 22–30 GHz. Vertical profiles of temperature and water vapor density are derived from the T_B values using a neural network retrieval scheme described in Solheim et al. (1998), trained with radiosonde data from Dodge City, Kansas. Integrated values of water vapor and cloud water are determined using the two-channel (23.8, 31.4 GHz) retrieval scheme of Hogg et al. (1983). The MPR vertical resolution and retrieval accuracy is discussed in Ware et al. (2005, manuscript submitted to *J. Appl. Meteor.*). Since vertical resolution scales with height, the best resolution is obtained at low levels. For example, at 2 km AGL the estimated vertical resolution for T and ρ_v is about 1.9 and 0.75 km, respectively. Instrument intercomparisons of retrieved temperature and water vapor have indicated that accuracy of microwave radiometer retrieved temperature is about 1 K near surface to 1.5–2.0 K above 2 km. Accuracy of retrieved water vapor was found to be 0.2–0.3 g m^{-3} near the surface and 1.0–1.5 g m^{-3} between 1 and 2 km AGL (Schroeder 1990; Solheim et al. 1998; Güldner and Spänkuch 2001; Ware et al. 2005, manuscript submitted to *J. Appl. Meteor.*).

Data from other IHOP platforms utilized in this study include Weather Surveillance Radar-1988 Doppler (WSR-88D), mobile Doppler radars [Doppler on Wheels (DOW); Wurman 2002)], dropsondes, Mobile GPS/Loran Atmospheric Sounding System (M-GLASS) sondes, and Geostationary Observational Environmental Satellite (GOES).

For convective initiation experiments, the typical strategy was to position the MIPS near the geometric center of the polygon (box or triangle) formed by three or four mobile Doppler radars. In all cases examined herein, the boundary translated over the MIPS while the Doppler radars and airborne instruments monitored airflow and thermodynamic conditions within and around the boundary zone.

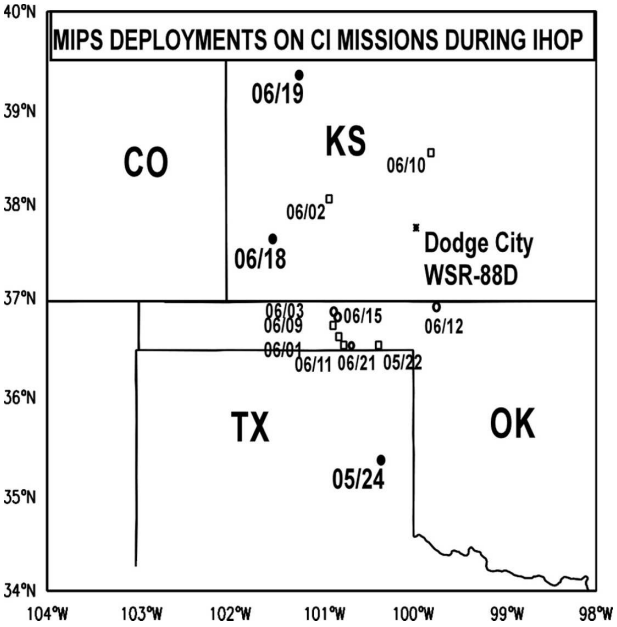

FIG. 2. Locations of the MIPS during convective initiation missions between 13 May and 25 Jun 2002 are shown. Open and filled circles are those that are included in Table 2. Filled circles are analyzed in the text. The rest of the CI missions are depicted with squares.

b. MIPS observed boundaries

The MIPS deployment locations for all IHOP CI missions are plotted in Fig. 2. A subset of these missions, in which CBZs passed over the MIPS, is summarized in Table 2. Measurements were acquired on two cold fronts, two drylines, a gust front, an outflow boundary, and a hybrid gust front/bore boundary. Variations in surface thermodynamic variables prior to and just after boundary passages are based on times of surface wind shifts. The surface wind vector change magnitude, $|\Delta \mathbf{V}_h|$, is computed by using representative wind vectors prior to and after boundary passages. An updraft threshold of 1.5 m s^{-1} is used to define CBZ updraft duration. Boundary layer heights were determined from a local maximum in 915-MHz profiler SNR, produced by Bragg scatter from mixing of air within the convective boundary layer (CBL) and drier air above the CBL (White et al. 1991; Grimsdell and Angevine 2002).

The CBZs listed in Table 2 were associated with peak updraft magnitudes of 3 to 8 m s^{-1}, updraft depths of 2–3 km, a maximum in CBL depth and precipitable

TABLE 2. A summary of MIPS observed boundaries. Long dash indicates that variable did not change significantly with boundary passage; $Z_{i\text{-bef}}/Z_{i\text{-aft}}$ represent boundary layer heights before and after boundary passages.

IHOP_2002 parameter	Days						
	24 May	3 Jun	12 Jun	18 Jun	19 Jun	15 Jun	21 Jun
Boundary type	Cold front		Outflow boundary	Drylines		Gust front	Gust front/ bore
$\Delta T/\Delta T_v$ (°C)	−2.8/−3	−1/−1.3	−2.0/−2.2	−5/−4.5	2/1.5	−8.5/−9.2	1/1
Δr_v(g kg^{-1})/ΔT_d(°)	1.3/2	−2.3/−4	2.2/3.0	4.5/6	−2.5/4	−1/−1	−1.9/−2.5
$\lvert\Delta V_h\rvert$ (m s^{-1})	11	6	7.5	7	7.5	16	4
Updraft duration (min)	5	1	5	2	7	8	1
Max updraft (m s^{-1})	4.5	5	5	5	6.2	8.3	3.4
$Z_{i\text{-bef}}/Z_{i\text{-aft}}$	1.5/2.0	1.0/1.5	1.9/2.2	1.3/2.0	1.3/2	1.2/ND	0.8/1.5
PW enhancement (mm)	+3.5	—	—	+7	+2	+8	+7
Cloud-base height (km)	1.5/2.0	No cloud	3.0/2.5	No cloud	3.2	2.2/1.4	2/1.3
Aerosol backscatter change	Increased	Increased	—	Increased	—	Increased	Increased

water (PW) within the CBZ, enhanced ceilometer backscatter within the cooler air mass adjacent to the CBZ, and large variations in surface properties (particularly mixing ratio) within the CBZ.

Clouds were not always present in the CBZs sampled. At one extreme, no clouds accompanied the CBZs on 3 June (a weak cold front) and 18 June (a retrograding dryline). At the other extreme, a cloud field 30 km wide accompanied the gust front/bore hybrid during the evening hours on 21 June. In three of the cases (18, 19, and 21 June), convective initiation occurred within 30 km of the MIPS location along the CBZ sampled by the MIPS. The following sections present more detailed analyses of the 19 June dryline, the 18 June retrograding dryline, and the 24 May shallow cold front. The 24 May and 18 June cases exhibit remarkable similarity in their resemblance of a gravity current flow. The gust front/bore hybrid sampled on 21 June is described separately in Knupp and Karan (2005, manuscript submitted to *Mon. Wea. Rev.*).

3. 19 June 2002 dryline

MIPS observations of a dryline were acquired 40 km east of Goodland, Kansas, between 1945 and 2125 UTC on 19 June 2002. The relative location of the MIPS is

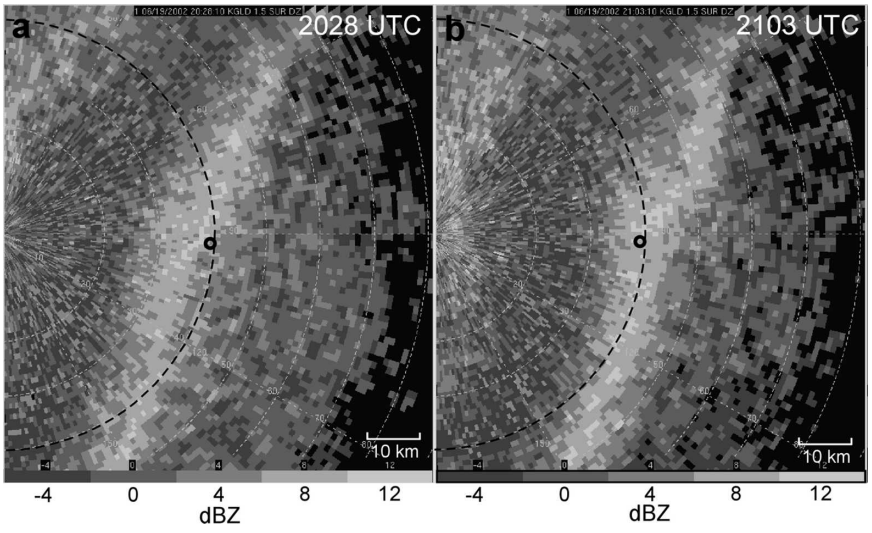

FIG. 3. Goodland, KS, WSR-88D reflectivity factor at 0.5° elevation angle before and after the dryline passage over the MIPS on 19 Jun 2002. MIPS location is denoted with a circle. Range rings are drawn every 10 km, beginning at 20 km. The 40-km range ring is the black dashed semicircle.

superimposed on reflectivity images from the WSR-88D located near Goodland (Fig. 3). The broad (10 km wide) radar fineline, defined by reflectivity factor (Z) in the range of 4–12 dB*Z*, was moving ESE at a relatively slow speed of 2–3 m s^{-1} during the observational period. Consequently, the MIPS remained within the boundary zone for about 30 min. As the dryline boundary passed over the MIPS, initial cumulus clouds formed to the west, and deepened immediately to the south and east, producing precipitation from cells located 20 km south-southwest of the MIPS location by 2122 UTC. This convective initiation occurred about 5 km in advance of the CBZ fine line. A detailed mesoscale analysis around the time of these observations is presented in Murphey et al. (2006).

a. Boundary layer kinematics

The dryline CBZ sampled between 2030 and 2100 UTC behaved as a transition zone between two boundary layers (Figs. 4a,b). The CBZ was marked with enhanced SNR at low levels (produced by Rayleigh and Bragg scatter[1]) and two prominent updrafts between 2030 and 2100 UTC. Assuming a fine line movement speed of 3 m s^{-1}, the line-normal width of the CBZ is estimated at 5–6 km, a value about one-half the Z fine line width in Fig. 3. The western edge of the dryline was marked with a sharp wind shift and weak flow after 2100 UTC. The CBL depth shows considerable temporal/spatial variability. In the moist air east of the dryline (before 2030 UTC) the depth appears oscillate between 2.3 and 3.2 km,[2] while in the drier air to the west (after 2100 UTC) the CBL depth was about 0.5 km deeper at 2.9–3.5 km (Fig. 4). The maximum height of the CBL exceeded 3.5 km (and extended above the height coverage of the 915-MHz profiler) within the western portion of the CBZ between 2045 and 2100 UTC. An east–west line of three dropsondes (not shown), released very close to the MIPS latitude between 2129 and 2135 UTC, corroborate these inferences. The dropsonde at 2122 UTC sampled near the center of the CBZ and revealed a 3.3-km-deep CBL, notably deeper than in the dry air 35 km to the west, or the moist air 35 km to the east.

Vertical profiles of horizontal flow (10-min averages) for the 2000–2120 UTC period are presented in Fig. 5. Prior to CBZ arrival at 2030 UTC, the airflow was uniform in direction (220°) and speed (15 m s^{-1}) within the lowest 2 km. By 2110 UTC, the wind direction below 2 km had veered to a westerly direction, and the wind speed had decreased to 5–7 m s^{-1}. Relatively weak signal within the 1.5–3.0-km layer, combined with strong turbulence, produced a rather noisy wind profile in this layer despite the 10-min averaging.

Surface time series during the CBZ passage (Fig. 6) reveal considerably more structure than the averaged winds from the 915-MHz profiler. Between 2030 and 2100, mixing ratio decreased from 9 to 7 g kg^{-1}, the wind direction shifted from 220° to 320°, and wind speed decreased from 9 to 5 m s^{-1}. Virtual temperature (T_v) exhibited several oscillations of about 1 K prior to and during the CBL passage. A net increase of 1 K was recorded across the boundary zone from the moist to dry air mass. Observational studies and modeled drylines exhibit a cross-dryline variation in T_v of 1 to 2 K, decreasing toward the moist BL (Parsons et al. 1991; Ziegler and Hane 1993; Ziegler et al. 1995; Ziegler and Rasmussen 1998). All parameters exhibit an oscillatory pattern within the boundary zone, indicative of the three-dimensional structure of large turbulent eddies suggested in the Z patterns of Fig. 3 (most likely cellular convection; see Weckwerth et al. 1999) that were superimposed on the CBZ updrafts (see Murphey et al. 2006).

Two sustained updrafts (updraft 1 and updraft 2) were measured within the CBZ (Figs. 4b and 6e). Both updrafts were clearly more significant than shorter-lived, weaker updrafts associated with CBL eddies prior to 2030 UTC. Updraft 1 (2037–2044 UTC) was more prolonged and was associated with 1 g kg^{-1} oscillations in surface mixing ratio and corresponding wind speed/direction changes (Figs. 6a,b). Scattered Cu clouds were associated with updraft 1, but PW from the MPR displayed a reduction from values east of the CBZ at 2025 UTC (Fig. 6d). We believe this is most likely due to the water vapor measurement from the MPR occurring prior to the arrival of this updraft. Updraft 2 was associated with enhancements in PW, which increased by 10% from 30.4 mm at 2039 (close to updraft 1) to 33.8 mm at 2053 UTC (Fig. 6d). The MPR sounding (Fig. 7) within updraft 2 shows an increase in mixing ratio from just above the surface to about 400 hPa and is consistent with the 2129 UTC dropsonde sounding within the CBZ 36 min later. Updraft 2 was associated with a well-defined surface wind shift (accompanied by dust devils), and more vigorous, growing

[1] The 915-MHz profiler is sensitive to Rayleigh scatter from insects, as well as Bragg scatter from refractive index irregularities at scales of one-half the radar wavelength (~16 cm).

[2] An enhancement in SNR is most sensitive to large vertical gradients in water vapor, and secondarily to temperature inversions (Angevine et al. 1993; Rogers et al. 1993; Grimsdell and Angevine 1998, 2002; Cohn and Angevine 2000). In this case, dropsonde data indicate large humidity gradients at the top of the ABL. Thus, the CBL top is below the maximum in SNR.

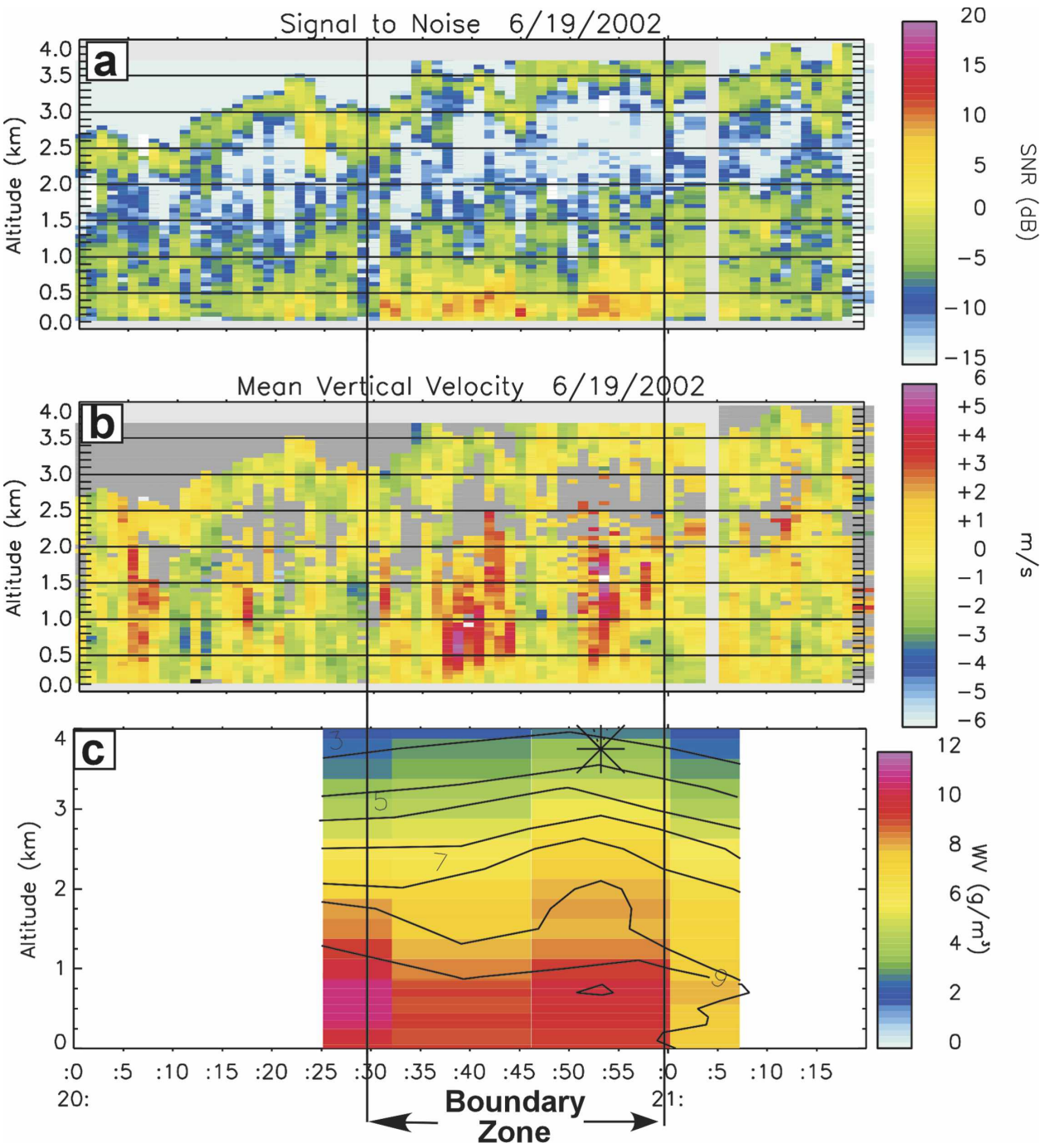

FIG. 4. Time vs height sections of 915-MHz profiler (a) SNR and (b) mean vertical velocities between 2000 and 2120 UTC on 19 Jun 2002, and (c) time–height section of retrieved water vapor density (g m^{-3}) from the MPR. The star depicts the estimated cloud base from the radiometer. Note that MPR data were not available prior to and after this time period.

Cu clouds that immediately preceded CI. Reductions in solar radiation were more substantial in advance of updraft 2 (Fig. 6c), indicating that more extensive and vigorous cumulus clouds had formed. At the time of this reduction (2045 UTC, or 1620 local solar time) the solar altitude was about 35°, and the pyranometer would have been shaded by clouds located about 5–6 km to the west. Murphey et al. (2006) found that updrafts were associated with misocyclones within the CBZ.

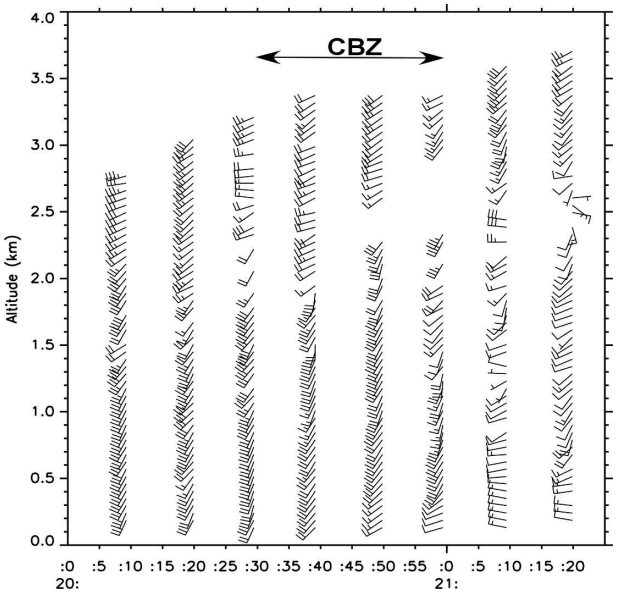

FIG. 5. Time–height section of 915-MHz-derived 10-min-averaged horizontal winds between 2000 and 2120 UTC from 0.110 to 3.6 km. Half barbs represent winds less than 2.5 m s^{-1} and full barbs are for 5 m s^{-1}.

b. Details of the vertical motion within the boundary zone

Figure 8 presents vertical profiles of Doppler velocity (W) and SNR (both at zenith) within the core regions of updrafts 1 and 2. Although both updrafts show a monotonic increase in W to peak values of 5–6 m s^{-1} at 1.0 and 1.6 km, respectively, appreciable structure is apparent in both updraft profiles. Assuming an incompressible atmosphere, the horizontal convergence implied by the average vertical gradient in W (below the maximum in W), $\Delta W/\Delta z$, is 6×10^{-3} and 4×10^{-3} s^{-1} at 2040 and 2054 UTC, respectively.

SNR values exhibit a primary maximum below 500 m, and a distinct secondary maxima at 3.3 and 3.5 km AGL, the latter likely produced by Bragg scattering associated with sharp mixing ratio gradients at the CBL top, consistent with the dropsonde measurements (not shown). Both updrafts extended to about 2 km, well below the measured cloud-base height and CBL top of 3.3–3.5 km. At 2054 UTC a secondary W maximum within a weak signal is apparent near 3 km. The LCL of surface parcels was about 3.4 km, close to the measured cloud-base height and CBL top. *Based on these data, we note that CI occurred when the CBL (mixed layer) extended to the LCL height of surface-based air parcels, in the presence of CBZ forcing (updraft).*

Doppler spectra from selected heights and times (2039, 2040, 2053 and 2054 UTC) are shown in Fig. 9 to illustrate the range of W values measured within the radar sample volume. (The 9° beam produces a transverse dimension of 230 m at 1.5 km AGL.) Doppler spectra yield insights on the extreme values of W measured during the 30-s dwell time. For each spectrum, the mean is marked with a vertical dashed line. Maximum values of W in each updraft approached 8 m s^{-1} at 2039 (0.5 km) and 2054 (1.5 km). Although most spectra assume a Gaussian shape, some exhibit a skewed distribution. Updraft 1 was stronger below 0.5 km AGL, but was weaker at higher altitudes. Updraft 2 was associated with a PW enhancement, and was more pronounced at higher altitudes with about a 3 m s^{-1} mean vertical velocity.

4. 18 June 2002 retrograding dryline

Ground-based systems deployed three times on 18 June 2002 to monitor a retrograding dryline over southwest Kansas. During the final deployment, the MIPS sampled (i) the dry (northwest) side of the retrograding dryline, (ii) the CBZ passage at 2248 UTC, and (iii) the more stable, moist air mass behind the CBZ. Figure 9 displays the DOW2 radar fine line patterns at 2245 and 2312 UTC. The CBZ motion vector was northwestward at about 9.5 m s^{-1}. Two convective cells, cell 1 (30 km north of the MIPS) and cell 2 (13 km northwest of the MIPS), intensified shortly after the CBZ intersected their location. The intensification of cell 1 occurred within a preexisting cumulus cloud field shown in the background of Fig. 1.

a. Boundary layer kinematics

Large eddies in the form of horizontal convective rolls (HCRs) were well formed in the ABL both ahead and behind the boundary. These are apparent as slightly wavy lines of enhanced Z, oriented north–south, in Fig. 10. The 915-MHz profiler measurements (Figs. 11a,b) indicate a turbulent CBL about 3 km deep between 2200 and 2240 UTC. Updrafts associated with HCRs, including one with a significant SNR enhancement at 2238 UTC, were sampled at rather regular intervals (10–15 min) prior to the CBZ passage. At 2245 UTC, the CBZ updraft is clearly portrayed in the 915-MHz SNR and W measurements. The primary updraft was located at the leading edge of the enhanced 915-MHz SNR and X-band radar fine line signatures (Fig. 10a). The CBZ updraft exhibited a maximum value of 4 m s^{-1} near 1.2 km AGL and extended upward to near 3 km AGL. Doppler spectra (not shown) indicate maximum updraft amplitude of about 5 m s^{-1}. The updraft duration was limited to 3 min due to the fast CBZ movement. The 3-min updraft duration implies an up-

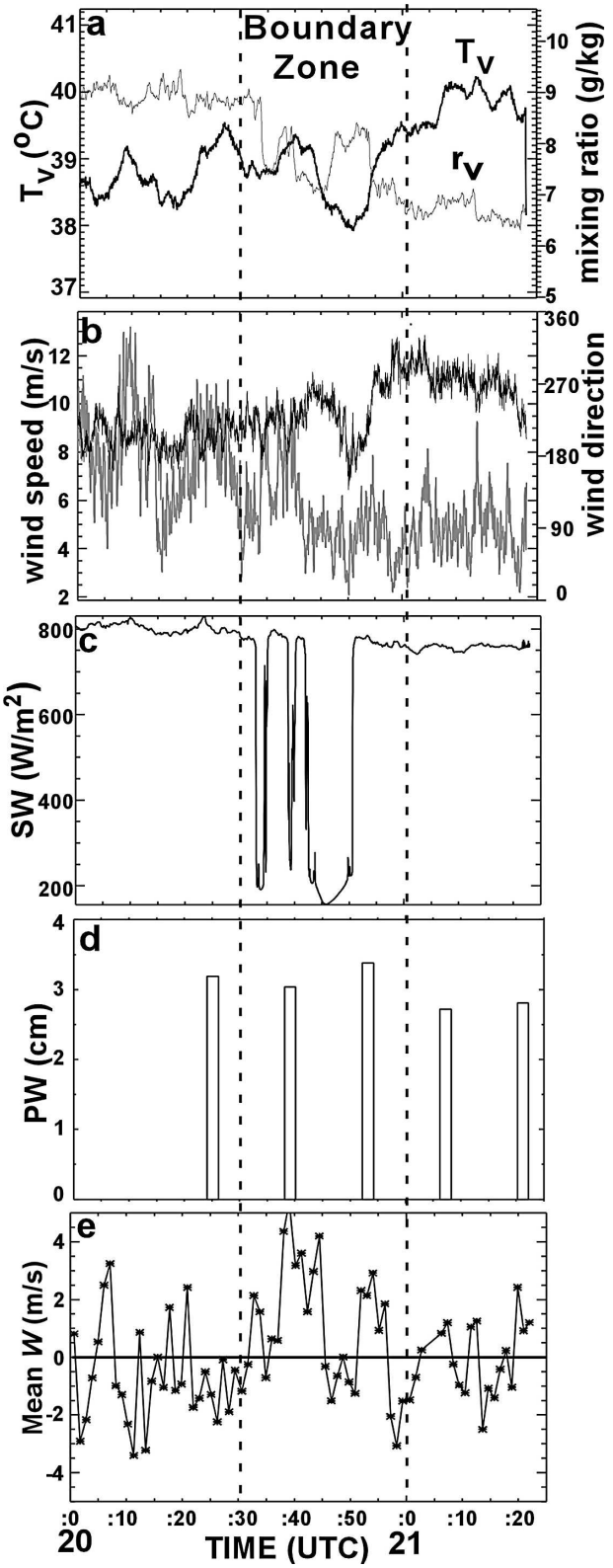

FIG. 6. (a)–(c) MIPS surface observations of (a) virtual temperature and mixing ratio (gray), (b) wind direction and wind speed (gray), (c) solar radiation, (d) precipitable water derived by the MPR, and (e) mean vertical velocities at 0.68 km AGL obtained from the 915-MHz profiler between 2000 and 2125 UTC on 19 Jun 2002.

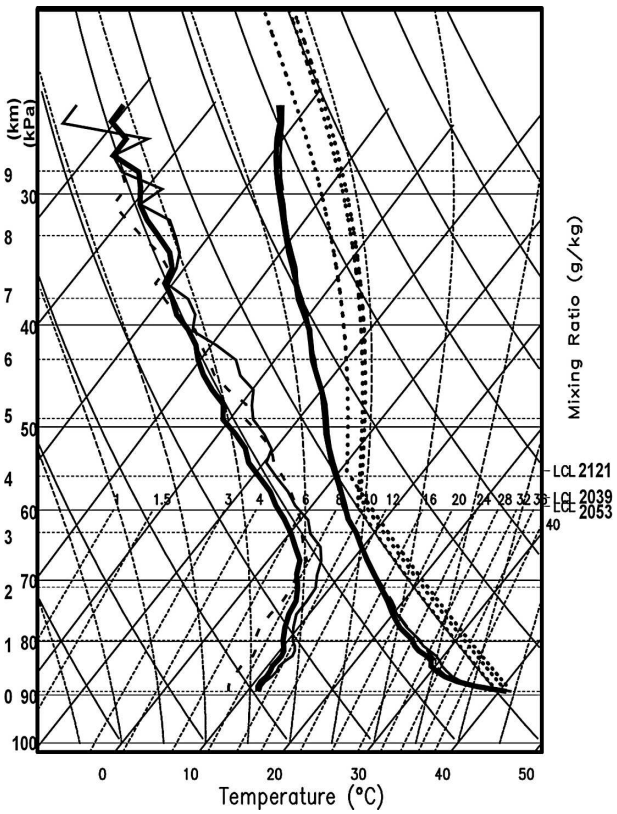

FIG. 7. Twelve-channel microwave-profiler-derived soundings at 2039 UTC east of the dryline (thick solid lines); 2053 UTC, within the dryline CBZ (medium thick solid lines); and 2121 UTC, west of the dryline (dashed lines). Surface-based LCLs are also depicted with their corresponding times.

draft width of about 1.7 km, assuming a CBZ movement speed of 9.5 m s^{-1}. A prolonged downdraft of 1–2 m s^{-1} magnitude immediately followed the CBZ updraft, and persisted for about 7 min below 1.5 km. Thereafter, the W field below 1.5 km AGL (within the stable air) remained rather benign.

Changes in surface thermodynamics were measured about 3 min after the updraft appearance. A very rapid increase in mixing ratio (8 to 12 g kg^{-1}), and a (less) rapid decrease in virtual temperature at 2247 UTC are depicted in Figs. 12a,b. These changes were accompanied by a 5 m s^{-1} increase in wind speed, but only a small change in wind direction. The total decrease in T_v of about 5°C over a 15-min time interval stabilized the ABL, which is readily apparent in the relatively quies-

←

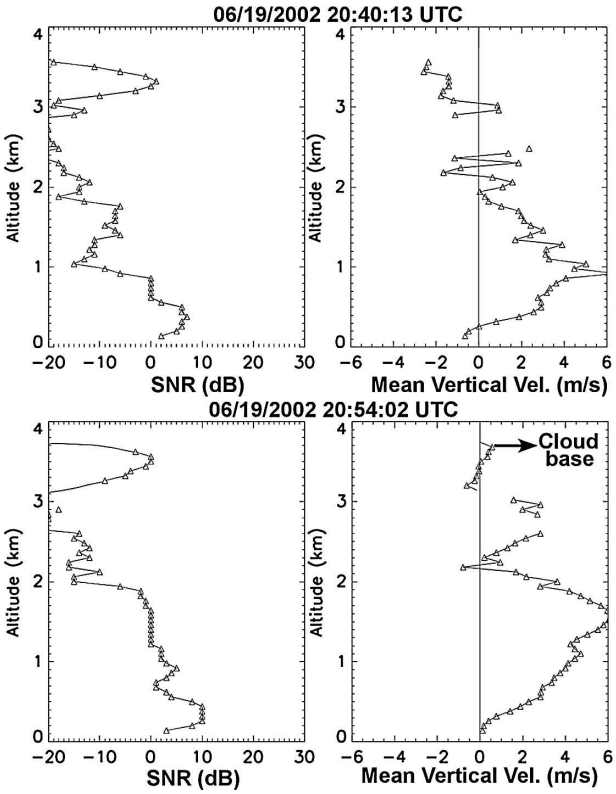

FIG. 8. Vertical profiles of SNR and mean vertical velocities at 2040 and 2054 UTC on 19 Jun 2002. Ceilometer-derived cloud-base height is also depicted.

cent *W* field (Figs. 11b, 12e) after 2300 UTC (which is somewhat surprising in view of the presence of HCRs). Cloud shading (as indicated by a significant reduction in solar radiation; Fig. 12c) from a small, high-based Cb immediately west of the MIPS contributed to the surface cooling and stabilization. In this case, the updraft occurred on the dry-air side of the CBZ and was lifted from near surface up to 2 km AGL. Although the LCL of surface air (see Fig. 14) decreased from 3.6 km in the warm, dry air to 2.4 km in the cooler, moister air, updrafts formed in the drier air mass. High cloud bases were noted (visually) below the developing convective clouds in the dry air mass.

Vertical profiles of horizontal wind (1 min) derived from the 915-MHz profiler portray a small change in wind direction, but a marked increase in wind speed below 1 km (Fig. 13) during boundary passage. The wind speed increased to 17–20 m s^{-1} over the lowest 1 km after the CBZ passage. Surface winds (Fig. 12b) also gusted to 18 m s^{-1} during this time. Wind direction and speed variations within the 2230–2245 UTC period correspond to HCRs (in advance of the CBZ) whose updrafts are recorded in Figs. 11b and 12e.

b. Thermodynamic characteristics

When compared to the 19 June dryline, the thermodynamic contrast at the surface in this case was certainly more substantial. The MPR time–height section

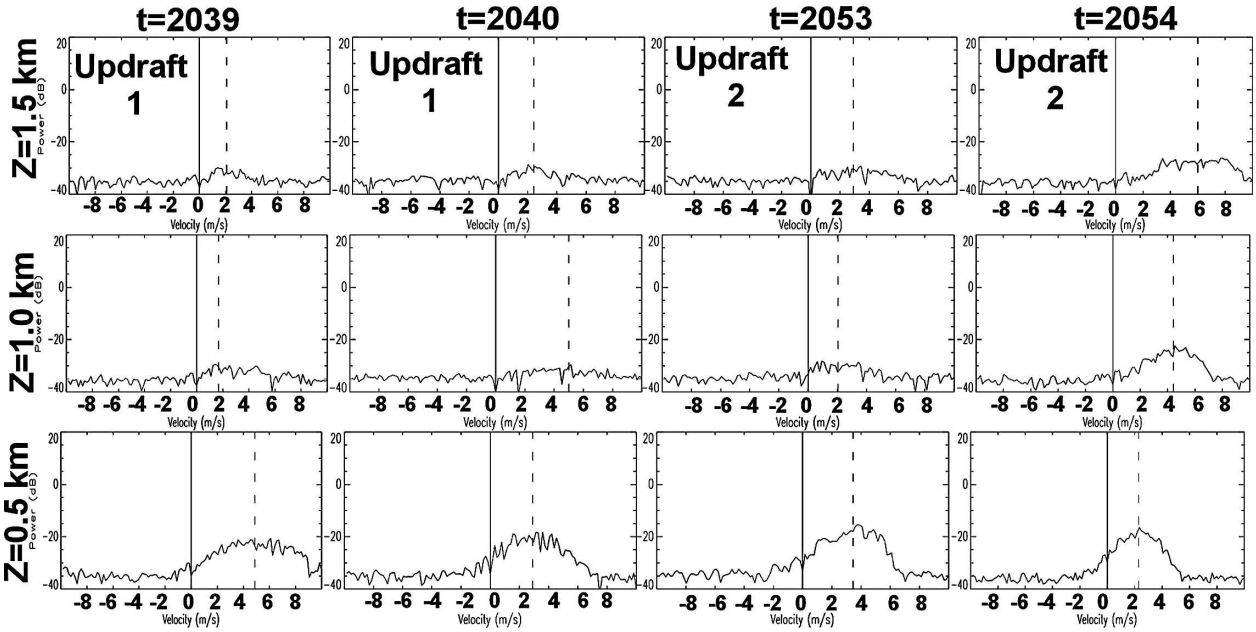

FIG. 9. Matrix of Doppler spectra for selected heights (0.5, 1.0, and 1.5 km) and times (2039, 2040, 2053, and 2054 UTC) on 19 Jun 2002. Vertical solid (dashed) line depicts 0 m s^{-1} (mean) velocity. Vertical velocity axis varies between −10 and 10 m s^{-1}.

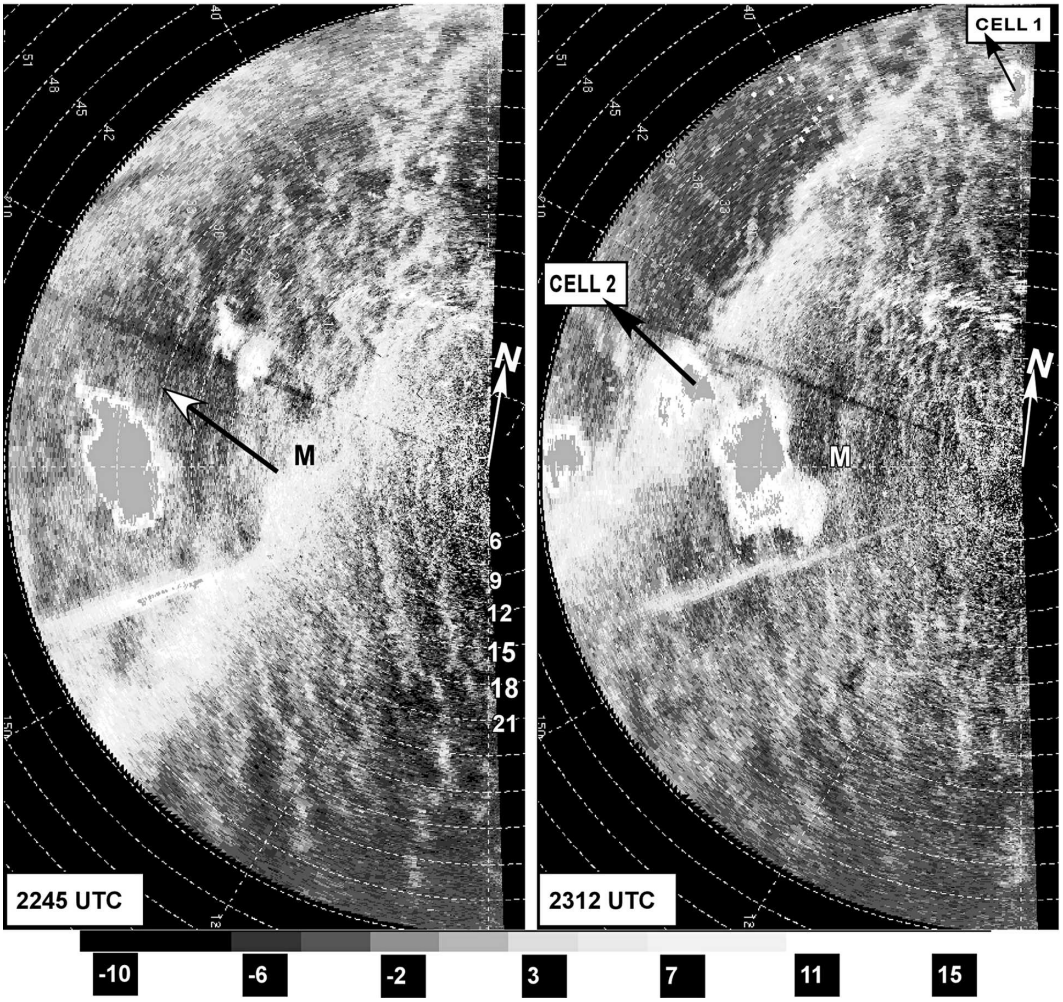

FIG. 10. Mobile X-band (DOW2) radar reflectivity factor at 1.5° elevation at 2245 and 2312 UTC 18 Jun 2002. The MIPS location is denoted with an M. Range rings are drawn every 3 km, beginning at 6 km. Arrow indicates direction of the boundary motion. The north is also depicted with an arrow and letter N.

(Fig. 11c) indicates that the most significant water vapor enhancement remained below 1 km AGL. The PW increased by 25% from 28 to 35 mm in the first sounding after CBZ passage (Fig. 12d). The MPR acquired only one observation within the dry CBL, as the first sounding (colored with black in Fig. 11d) was acquired before complete radiometer warm up. The 2237 UTC MPR sounding prior to the arrival of the CBZ (dashed lines in Fig. 14) indicates T and T_d of 38° and 10°C, respectively, at the surface, and a superadiabatic profile at low levels. The sounding immediately after the CBZ passage at 2252 UTC (long-dashed lines in Fig. 14) shows cooling confined to the lowest 2.0 km, and significant moistening up to 600 hPa (3 km AGL), which is consistent with the 3-km-deep updraft. The MPR sounding at 2306 UTC (solid lines) reveals similar cool, moist surface conditions, but warming and drying from just above the surface to about 670 hPa. This is physically consistent with prolonged subsidence after CBZ passage, portrayed in Fig. 11b.

The ceilometer detected enhanced backscatter associated with the arrival of cool air behind the CBZ near 2248 UTC (Fig. 11d), coincident with the moistening and cooling at the surface. Clouds were not detected, nor were they observed visually at zenith during boundary passage over the MIPS. (However, an existing precipitating convective cloud did cast a shadow over the MIPS.) This enhancement in return signal persisted in the lowest 1.5 km (the approximate depth of the cool air) between 2248 and 2320 UTC, with greatest increase during the period of downdrafts behind the CBZ between 2248 and 2300 UTC. As indicated in Table 2, CBZ passages are often accompanied by changes in ceilometer backscatter in contrasting air masses.

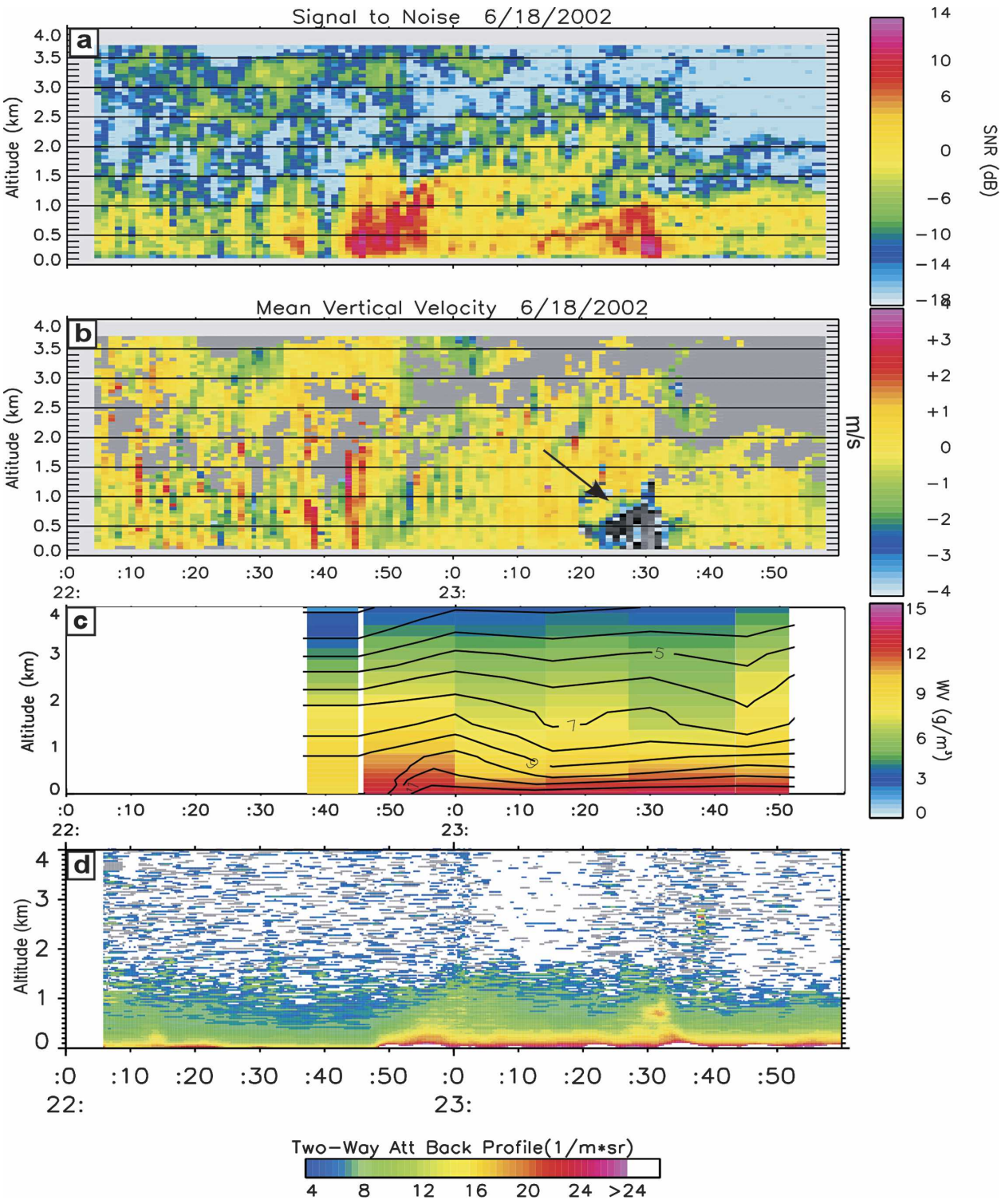

FIG. 11. Time vs height sections of 915-MHz profiler (a) SNR and (b) mean vertical velocities, (c) water vapor density derived from the MPR, and (d) ceilometer two-way attenuation backscattering during a retrograding dryline passage on 18 Jun 2002. The large-magnitude negative *W* values between 2320 and 2352 UTC (shown by an arrow) were produced by very light rain.

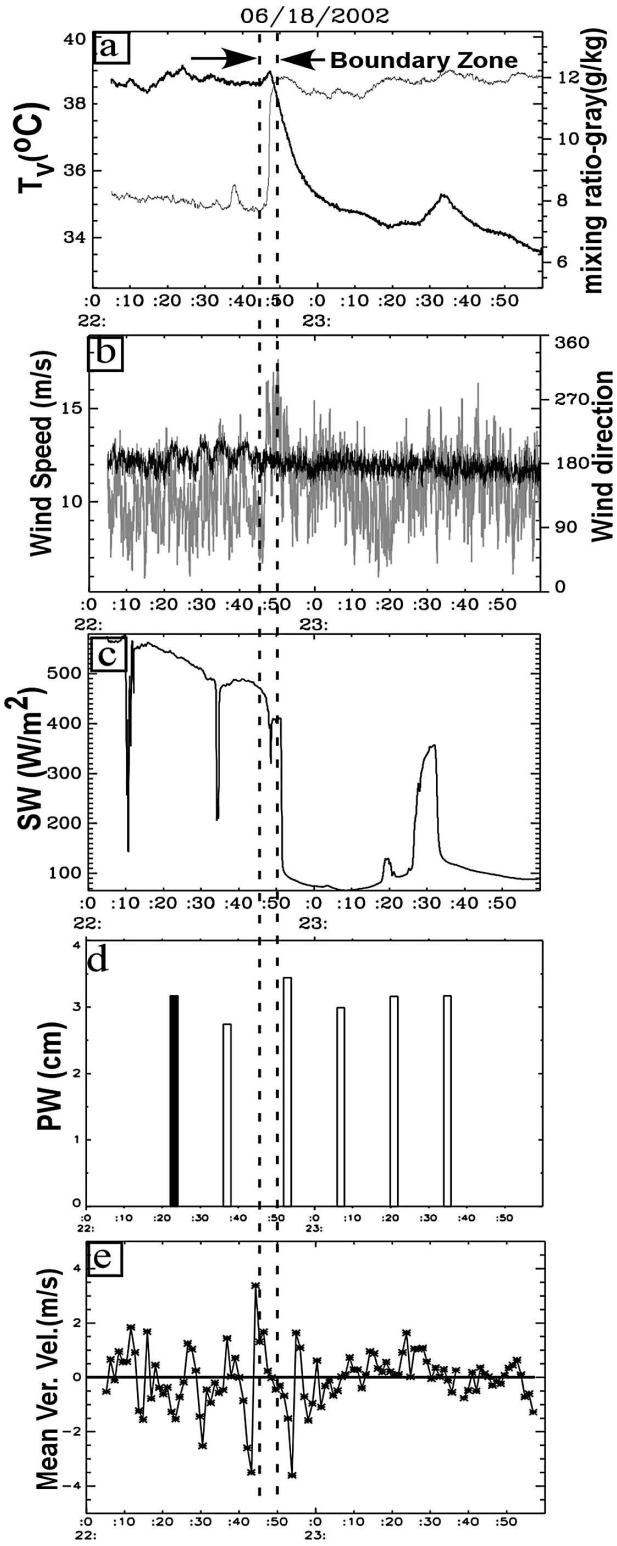

FIG. 12. MIPS surface observations of (a) virtual temperature and mixing ratio (gray), (b) wind direction and wind speed (gray), (c) solar radiation, (d) precipitable water derived by the MPR, and (e) mean vertical velocities at 1.28 km AGL, obtained from the 915-MHz profiler on 18 Jun 2002.

The internal Froude number (Fr, ratio of the inertial force to the force of gravity) is used to determine dynamical similarity to density currents (Wakimoto 1982; Kingsmill and Crook 2003; Parsons et al. 1991; Atkins et al. 1998). For a sample of 10 gust fronts and see-breeze fronts, Kingsmill and Crook (2003) found that Fr varied between 0.7 and 1.4, and 0.5 and 1.0, for gust fronts and see breeze fronts, respectively. Herein, to compute the Fr, we adopted the same procedure that Kingsmill and Crook (2003) used. Cold and moist flow in Fig. 11c is confined from surface to about 500 m AGL. Average virtual potential temperatures acquired from MPR within the 500-m depth of the ambient air (west) and air behind (east) the retrograding dryline, and dryline propagation speed of 9.5 m s^{-1} yield a Fr of 0.6. This value is close to the lower limit of Fr range for the sea-breeze fronts (Kingsmill and Crook 2003).

5. 24 May 2002 shallow cold front

A convective initiation mission was conducted in the vicinity of a cold front, a dryline, and their triple point located over the Texas panhandle on 24 May 2002. A detailed mesoscale analysis of this event is presented in Wakimoto et al. (2006). Boundary locations and radar fine line measurements (Fig. 15) from the DOW radar indicate a southeastward propagation of the cold front and a slow eastward advance of the dryline. The triple point intersection progressed rapidly southward because of the faster movement speed of the cold front. The MIPS observations captured only the cold-frontal passage and the evolution of the cloud-topped CBL prior to the cold-frontal passage. Convection initiation occurred after 2000 UTC greater than 50 km to the south and east of the MIPS. Wakimoto et al. (2006) and Geerts et al. (2006) describe other features of this case.

a. Boundary layer properties prior to cold-frontal passage

Pre-cold-frontal CBL properties between 1820 and 2000 UTC are depicted by the 915-MHz SNR and *W* in Figs. 16a and 16b. Distinct turbulent eddies are apparent within the CBL from 1820 to 2000 UTC. Peak updrafts and downdrafts were about 2 m s^{-1}, and the strongest magnitudes (~2 m s^{-1}) were limited in duration to about 1 min. The CBL top, inferred from the height of SNR relative maxima within the 1.6–2.8-km layer, increased from near 1.7 km at 1820 UTC to 2.4 km by 2000 UTC. A 1920 UTC M-GLASS sounding

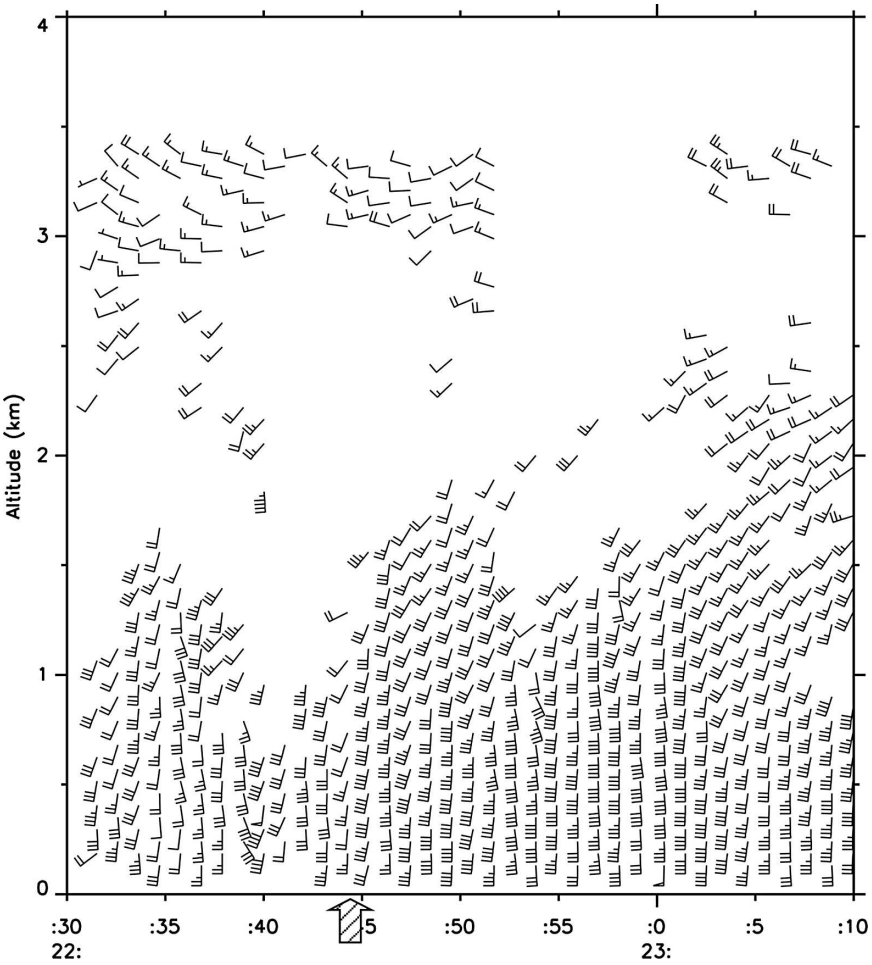

FIG. 13. Time vs height section of 915-MHz 1-min-averaged horizontal winds between 2230 and 2310 UTC on 18 Jun 2002 from 0.110 to 3.4 km. Half barbs represent winds less than 2.5 m s^{-1} and full barbs are for 5 m s^{-1}. The wide arrow at 2244–2245 UTC depicts the time of the CBZ updraft.

(Fig. 17a) within the dryline boundary zone (the region where DOW X-band radar indicated rather diffuse localized high-reflectivity factors; not shown), and 7 km northwest of the MIPS (see Fig. 15a for location), shows a well-mixed CBL with a 2.2-km depth. This sounding exhibits a sharp gradient in mixing ratio centered near 2.4 km AGL. The peak in 915 SNR at 2.3 km corresponds to the level of this gradient. The CBL is marked by variability in wind speed and direction (Fig. 18), while more uniform flow and greater shear is located above CBL top (2 km), in agreement with the 1920 UTC sounding (Fig. 17a).

The ceilometer backscatter (Fig. 16c) indicates that cumulus clouds were common between 1820 and 2000 UTC. Cumulus bases increased from 1.5 km at 1825 UTC to 2.0 km at 1955 UTC. An increase in surface temperature and a slight decrease in mixing ratio from 1840 to 1950 UTC increased the LCL of surface-based air parcels from 1.8 to 2.2 km over this same time period. Figure 16a includes a plot of ceilometer cloud base (black dots) superimposed on the 915 SNR. We note that minimum cloud-base height was several hundred meters below the top of enhanced SNR, which defines the CBL top. Since minimum cloud-base heights were lower than the CBL top, we infer that these clouds were positively buoyant. The 915-MHz SNR shows evidence of individual Cu clouds as upward bulges of minimum detectable SNR. The estimated cloud depth (determined from the difference in maximum height of detectable SNR and minimum cloud-base height) increased from about 500 m at 1825 UTC to 800–900 m at 1950 UTC. The combined information in Fig. 16a suggests that the Cu clouds tilted downshear (consistent with the wind profile in Figs. 16a and 17), and exhibited

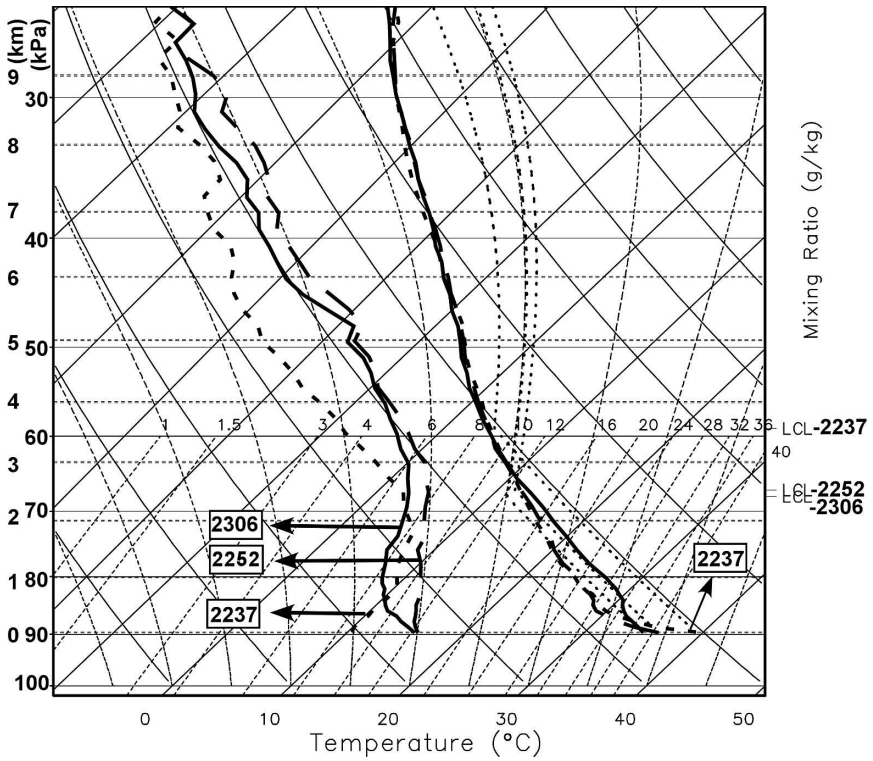

FIG. 14. Soundings, derived from 12-channel microwave radiometer, at 2237 (dashed), 2252 (long dashed), and 2306 UTC (solid). LCL of surface-based parcel for each sounding is shown on the right.

a minimum cloud-base height (and 1–2 m s^{-1} updrafts) on their upshear side. This latter facet was inferred from the lowest cloud base being measured after the maximum vertical extent of the 915 SNR.

Precipitable water values increased gradually by 12% from 24.4 to 27.9 mm during the observational period. Such an increase implies moisture convergence, which is corroborated by the Electra Doppler Radar (ELDORA)

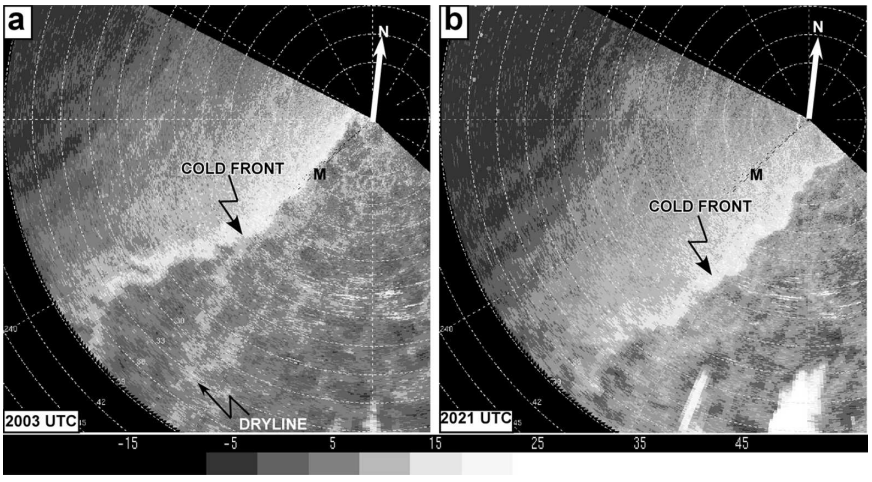

FIG. 15. Mobile X-band (DOW2) radar reflectivity factors at 1.4° elevation at (a) 2003 and (b) 2021 UTC 24 May 2002. The MIPS location is denoted with an M. Range rings are drawn every 3 km, beginning at 6 km.

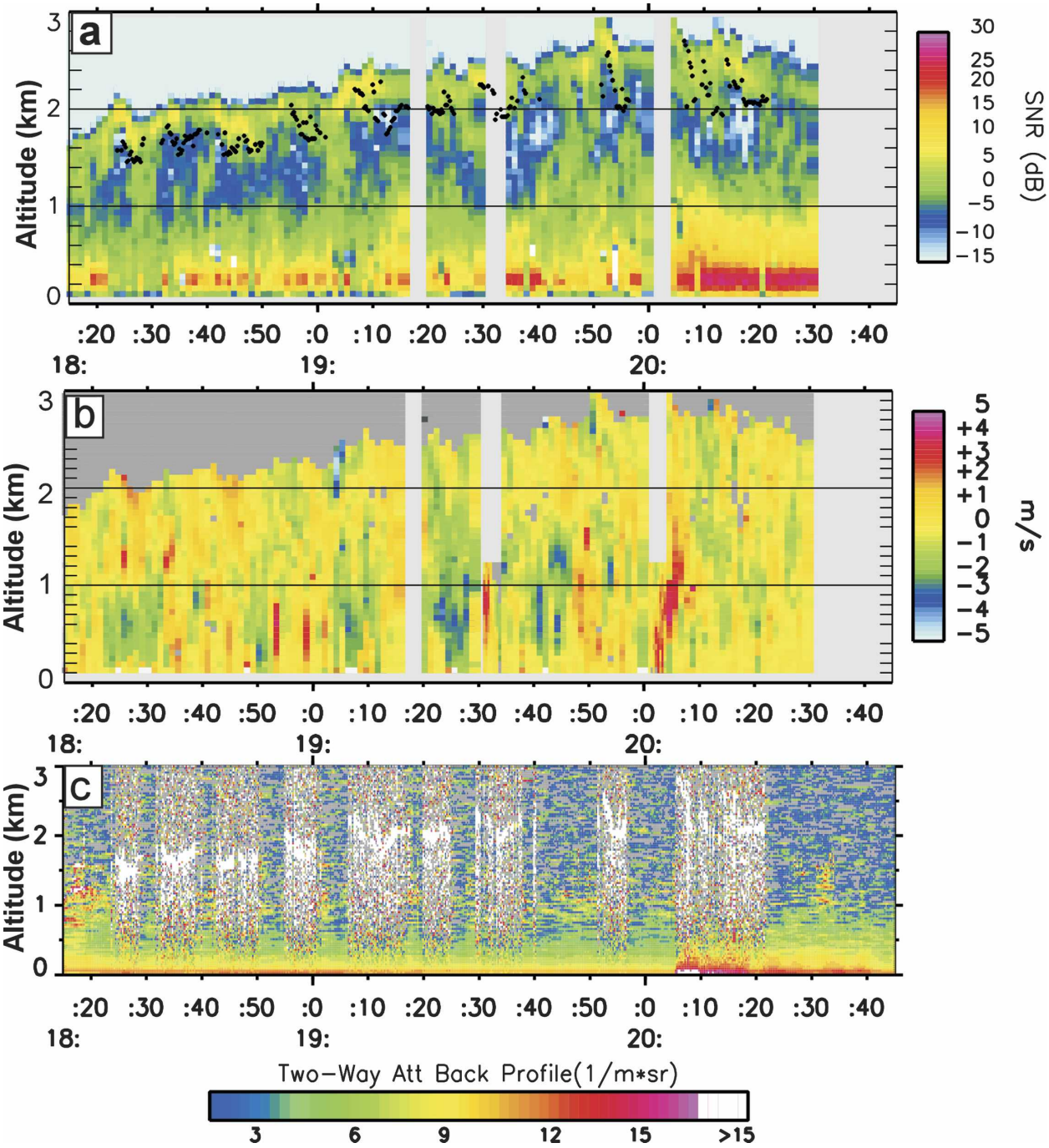

FIG. 16. Time–height sections of 915-MHz profiler (a) SNR, (b) mean vertical velocities, and (c) ceilometer two-way attenuation backscattering between 1815 and 2045 UTC on 24 May 2002. Cloud-base heights derived from the ceilometer are plotted as black dots in (a).

radar analysis in Wakimoto et al. (2006, their Fig. 4). Precipitable water was enhanced by only 1 mm (~4%) during the CBZ passage, which compares to 10% for 19 June and 25% for 18 June. Since the updrafts were confined to the CBL, where water vapor mixing ratio was well mixed, a significant enhancement in PW would not be expected even for a prolonged updraft that does not extend above the CBL top.

b. *Cold-front characteristics*

The cold-front boundary was relatively straight along its leading edge within 6 km of the MIPS. Bulges

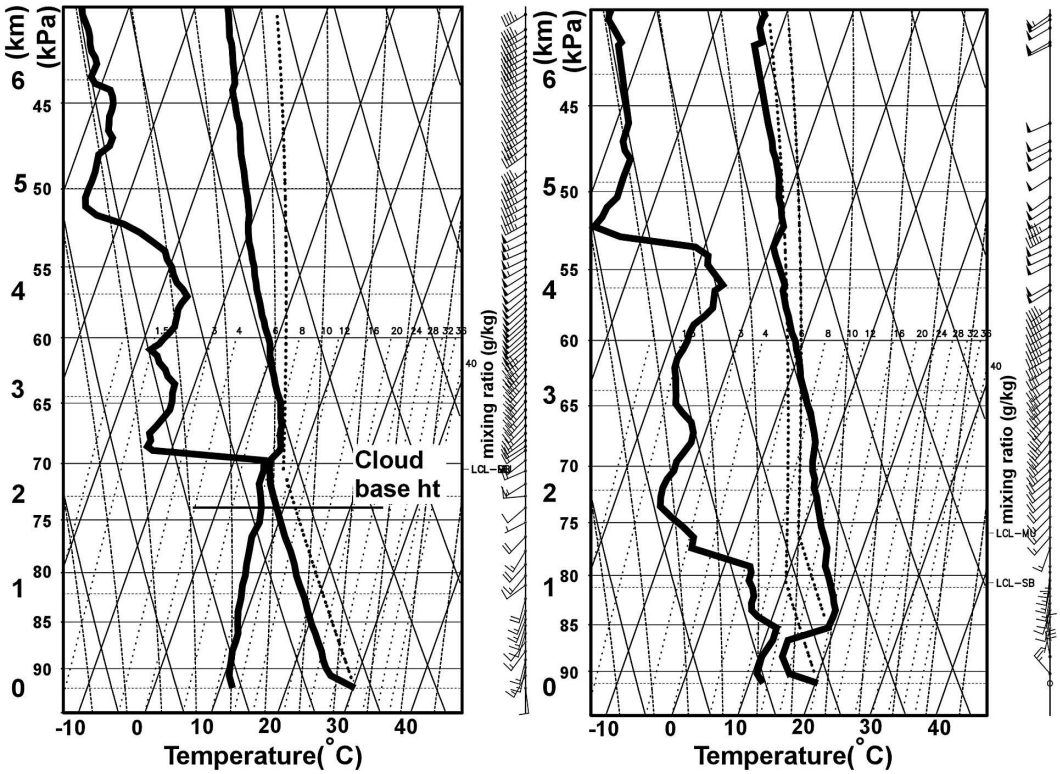

FIG. 17. M-GLASS sounding released at (left) 1920 UTC ahead of and (right) 2054 UTC behind the cold front on 24 May 2002. Height (AGL) and surface-based LCL are shown on the left and right.

formed at other locations and times, for example, southwest of the MIPS during time of passage (Fig. 15), and also 18 min later southeast of the MIPS. Reflectivity factor values were largest near the CBZ leading edge, tapering to background values within 6 km behind the leading edge.

A distinct surface wind shift and wind speed increase (Fig. 19b) accompanied the frontal passage. Southerly flow of about 4 m s^{-1} veered to 8 m s^{-1} northerly flow after the frontal passage. Both the wind direction and wind speed changes started at 2003 UTC, about 2 min before surface thermodynamic changes. A corresponding 0.2-hPa jump in surface pressure (not shown) was measured at the time of the updraft and is consistent with a dynamically induced pressure increase similar to that observed ahead of gust fronts by Wakimoto (1982). The magnitude of the wind vector change across the CBZ was relatively large, about 11 m s^{-1}. Assuming a CBZ movement speed of 5 m s^{-1}, the 5-min wind shift period corresponds to a CBZ width of about 1.5 km and an implied mean convergence of about 7×10^{-3} s^{-1}.

During the wind shift period, virtual temperature and mixing ratio changed by -3°C and $+1.3$ g kg^{-1}, respectively (Fig. 19a). As in the previous cases, the mixing ratio change was more rapid than the T_v change. A significant increase in ceilometer backscatter over the lowest 800 m coincided with arrival of the cool, moist air behind the cold front (Fig. 16c). The 2054 UTC M-GLASS postfrontal sounding (Fig. 17b) indicates that the depth of cold air behind the front was rather shallow at about 800 m.

A careful analysis of the 915-MHz profiler horizontal winds (Fig. 18) indicates that the deepest part of the cold front was the "head" structure, extending to about 1.1 km at 2010 UTC. Thereafter, the depth of the cool northerly flow decreased to 800 m by 2030 UTC, a value that is corroborated by enhanced ceilometer backscatter and enhanced 915-MHz SNR over this layer (Figs. 16a,c) and the postfrontal sounding in Fig. 17b.

Figure 18 shows southerly ground-relative airflow with speed of about 8 m s^{-1} prior to the cold front. This translates -4.2 m s^{-1} flow perpendicular to the front. For a boundary propagation speed of 5 m s^{-1}, a frontal depth of 700 m and a virtual potential temperature reduction of 2 K yield a Fr of 1.4. This value corresponds to the upper limit of observed F_r for gust fronts (Kingsmill and Crook 2003).

The updraft (temporal) structure shown in Fig. 16b suggests a pronounced geometric tilt of the updraft to-

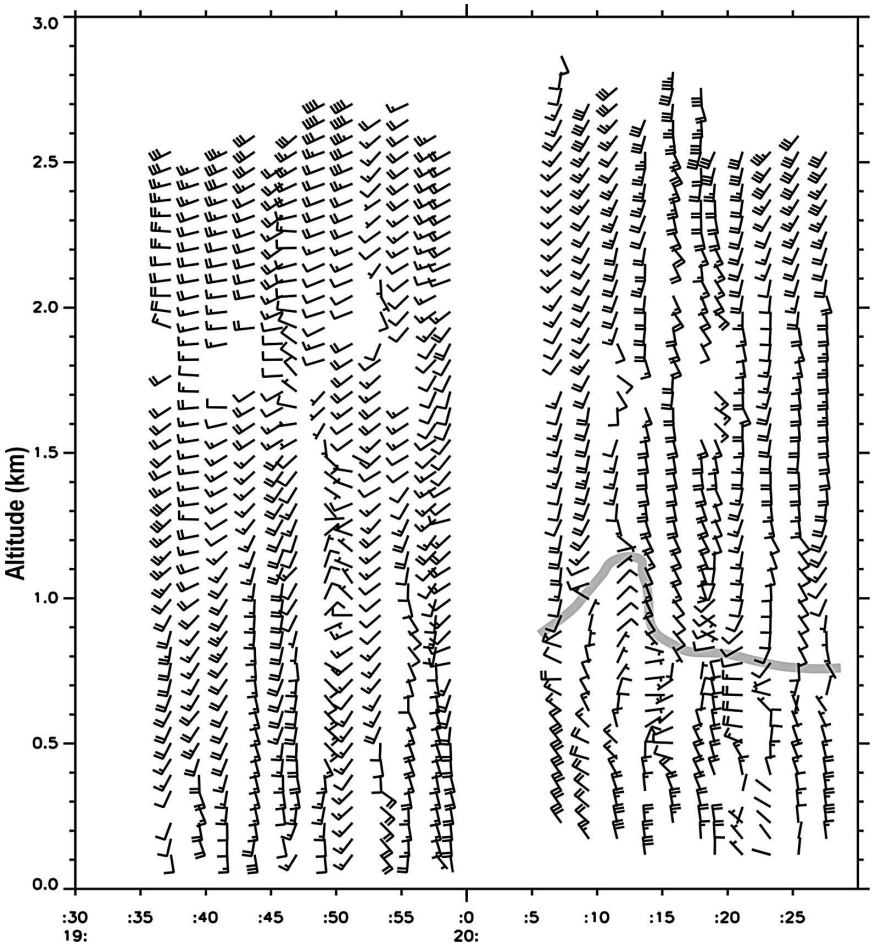

FIG. 18. Time–height section of 2-min-averaged 915-MHz profiler horizontal winds from 1935 to 2030 UTC on 24 May 2002. Full barbs are 5 m s^{-1}. Gray-shaded region depicts the intersection zone between the ambient and cold air.

ward the cool air behind the boundary, a property not observed in the previous two dryline cases. Such a tilt is consistent with the Rotunno–Klemp–Weisman (RKW) theory (Rotunno et al. 1988; Weisman and Rotunno 2004), which predicts a tilt toward the cool air mass when weak shear exists. The updraft was surface rooted with magnitude of 2 m s^{-1} at the 120-m AGL level at 2003 UTC. The cold-frontal updraft, notably different in structure from earlier CBL eddy updrafts, extended upward to about 2 km AGL by 2007 UTC.

Weak downdraft pockets were measured below 1 km, one immediately following the low-level cold-frontal updraft. The W time series at 0.67 km (Fig. 19e) shows the primary CBZ updraft followed by three $\pm$1–2 m s^{-1} oscillations in W with a 6–7-min period. The vertical gradient of potential temperature, $\Delta\theta/\Delta z$, associated with a Brunt–Väisälä frequency corresponding to this period is approximately 1 K (100 m)$^{-1}$. The center height of these oscillations is close to the 700-m height of the frontal inversion, where such a gradient appears to exist.

Profiles of W and SNR within the updraft are presented in Fig. 20 for two consecutive vertical samples (30-s dwell times for each, spaced in time by 60 s) at 2005–2006 UTC. The updrafts have a maximum value of about 4 m s^{-1} near 0.7–0.9 km (near the top of the cold front), and weaker downdraft (within the cool air) below 0.3–0.4 km. Such vertical stretching implies appreciable horizontal convergence near the 0.4-km level. Horizontal divergence for an incompressible fluid $[\nabla \cdot V_H + (\partial w/\partial z) = 0]$ at a specific atmospheric layer can be estimated by computing $\Delta w/\Delta z$ for specific layers. The maximum and minimum velocities at 2005 UTC (Fig. 20b) were 4.2 and -1.7 m s^{-1} at respective heights of 0.67 and 0.317 km. This yields a horizontal convergence estimate of 16×10^{-3} s^{-1}. At 2005 UTC, the updraft extended to about 2 km, well beneath the boundary layer height of 2.5 km AGL, estimated from

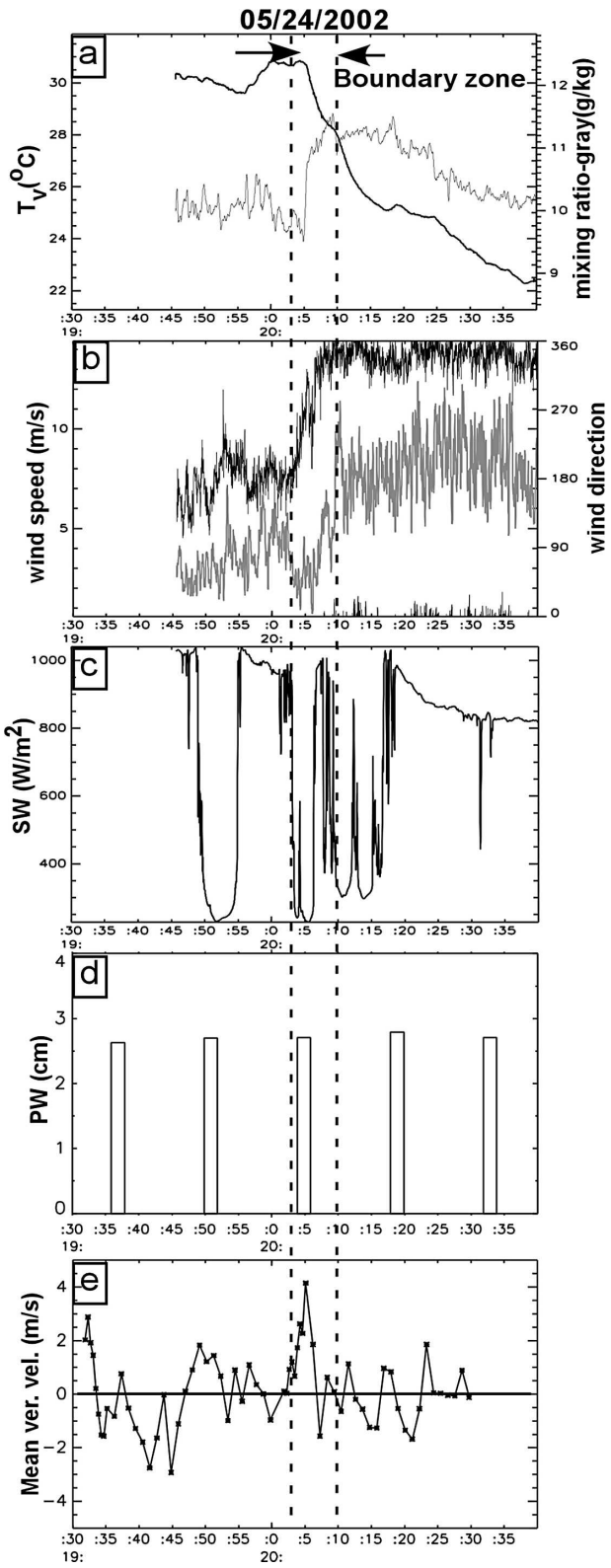

FIG. 19. MIPS surface observations on 24 May 2002. (a) Virtual temperature and mixing ratio (gray), (b) wind direction and wind speed (gray), (c) solar radiation, (d) precipitable water from the MPR, and (e) time series of 915-MHz profiler mean vertical velocities at 0.67 km AGL.

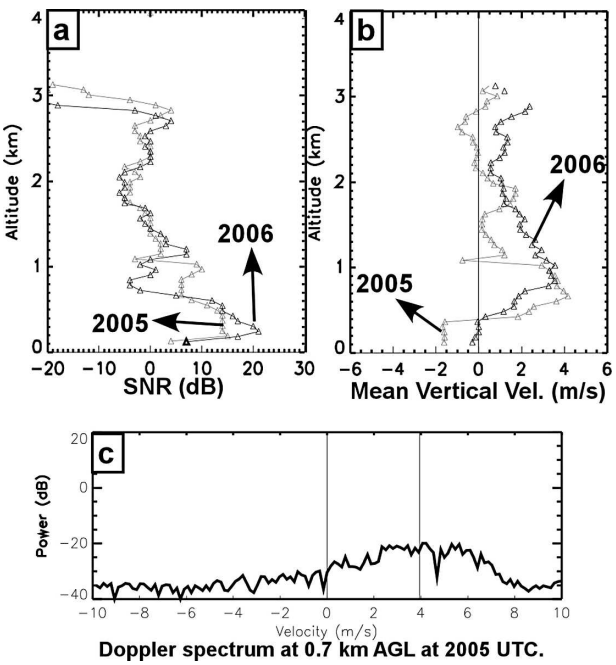

FIG. 20. Height profiles of (a) SNR and (b) mean vertical velocities at 2005 UTC (gray) and 2006 UTC (black), respectively. (c) Doppler spectrum at 0.7 km AGL at 2005 UTC.

the SNR maximum at 2.5 km. However, at 2006 UTC, the updraft appeared to extend to near 3 km, within cloud that had a base near 2 km and a top near 3 km. The Doppler spectrum at 0.7 km (Fig. 20c) suggests peak (turbulent) updraft speeds as high as 6–7 m s^{-1} at 0.67 km AGL.

c. *Absence of CI*

With regard to CI, this was a null case, even though Cu clouds with depths of 800–900 m existed in the vicinity of the MIPS. The ground-based observations yield three important clues that may explain the absence of CI:

(i) The weak inversion at the top of the CBL (Fig. 17a) reduced parcel buoyancy.
(ii) Significant vertical shear existed within the cloud layer at the CBL top (Fig. 18). Cloud modeling studies (Cotton and Tripoli 1978; Reuter and Yau 1987) have shown that vertical shear increases entrainment, which would have further reduced parcel buoyancy.
(iii) The front was shallow, having a maximum depth that was about one-half the CBL depth.

It seems plausible that all three factors contributed to the conditions that proved adverse to CI. The observations suggest that the atmosphere above the CBL and

CBZ was not modified (moistened) as in the 19 June case.

6. Summary and conclusions

a. General summary

During IHOP, the MIPS sampled the kinematic and thermodynamic properties of various convergent boundary zones (CBZs), including two cold fronts, two drylines, one vigorous gust front, and a hybrid gust front/bore, at high vertical and temporal resolution. Boundary layer properties in close proximity to other CBZs were also measured. The measurements revealed the following general properties:

- Updrafts for all boundaries varied from 3 to 8 m s^{-1}, with the maximum 8 m s^{-1} measured in a vigorous gust front.
- For the CBZs sampled within a convective boundary layer, the updraft magnitude and duration was about a factor of 2 greater than updrafts associated with boundary layer eddies.
- Enhanced Z (associated with the radar fine line) detected by the 915-MHz profiler was found to be much wider than the updraft, by about a factor of 5.
- CBZ updraft widths and depths were generally 1–2 and 2–3 km (close to the CBL depth), respectively.
- A local maximum in CBL depth usually accompanied the slower-moving CBZs.
- An enhancement in integrated water vapor was generally, but not always, associated with updrafts within the CBZ.
- Strong signals in ceilometer backscatter were usually associated with cool, moist air behind CBZs that exhibited gravity current characteristics.

b. Significant findings from detailed analyses of three CBZs

On 19 June, measurements of a slow-moving (3 m s^{-1}) dryline were acquired. During its passage over the MIPS, two main updrafts were sampled and significant variations in all surface parameters during the 30-min period were recorded. The net changes in surface parameters across the CBZ included an increase in T_v of 1 K, a 2 g kg^{-1} reduction in mixing ratio, and a 100° veering in wind direction.

The first updraft had maximum 5 m s^{-1} amplitude, but was relatively shallow at 2 km. The summit of the first updraft remained 1 km below the CBL top; hence, it was not associated with water vapor enhancements. The second updraft (6 m s^{-1}) was measured closer to growing Cu clouds exhibiting a deeper circulation, and a more significant (25%) PW enhancement. The maximum CBL height of 3.5 km AGL was measured within the CBZ. In this case, CI occurred when the CBL (mixed layer) extended to the surface LCL, in the presence of CBZ forcing (updraft) and water vapor enhancements within and above the CBL.

On 18 June, a retrograding dryline exhibited a peak updraft value of 4 m s^{-1} and a depth of 3 km, comparable to the CBL depth. Strongest winds of 15–20 m s^{-1} were measured within the ABL, below 1 km, on the cool side of the CBZ. Hence, horizontal convective rolls were common in the CBL. At the surface, T_v decreased by 1.5 K, and r_v increased very quickly by 4 g kg^{-1} as the retrograding dryline passed over. Thermodynamic characteristics derived from MPR, combined with the surface measurements, indicate that the dryline resembled a density current with an elevated head and an equilibrium depth of about 1 km (Charba 1974; Wakimoto 1982; Droegemeier and Wilhelmson 1987; May 1999). Calculated internal Froude number is found to be close to F_r numbers of sea-breeze fronts. The PW enhancement in this case was about 10% within/near the CBZ updraft.

On 24 May, measurements of a shallow cold front revealed sharp changes in surface properties: a change in magnitude of the wind vector of about 8 m s^{-1}, a decrease in T_v of -3 K, and an increase in r_v of +1.5 g kg^{-1}. The updraft exhibited a depth of about 2 km, a notable slope toward the cool air, and a peak magnitude of 4 m s^{-1} near 700 m (the top of the front). The leading edge of the front exhibited a well-defined head near 1.2 km AGL, and was capped by a sharp temperature inversion, located near 700 m AGL behind the surface front. Strong convergence of 16×10^{-3} s^{-1} near the 400 m AGL level was associated with a distinct frontal surface. This cold front also exhibited a close resemblance to a gravity current structure with Froude number of 1.4.

In this case, the absence of CI close to the MIPS location could be explained by a combination of three factors:

- A weak inversion existed at CBL top (but was not impermeable to parcels ascending from below).
- Significant vertical shear was located above the CBL.
- The shallow nature of the front (<1 km deep) limited the updraft depth, and hence the depth of water vapor enhancement.

Acknowledgments. Sincere thanks are extended to Justin Walters for programming assistance, to Dr. Yvette Richardson (Penn State University) and Dr. Josh Wurman for providing DOW radar data, and to all

IHOP investigators whose collaborative spirit and dedicated efforts made the IHOP field campaign a success. Comments by reviewers significantly improved the manuscript. This research has been funded by the National Science Foundation under Grants ATM-0002252 and ATM-0130611.

REFERENCES

Angevine, W. M., S. K. Avery, and G. L. Kok, 1993: Virtual heat flux measurements from a boundary-layer profiler–RASS compared to aircraft measurements. *J. Appl. Meteor.,* **32,** 1901–1907.

Atkins, N. T., R. M. Wakimoto, and T. M. Weckwerth, 1995: Observations of the sea-breeze front during CaPE. Part II: Dual-Doppler and aircraft analysis. *Mon. Wea. Rev.,* **123,** 944–969.

——, ——, and C. L. Ziegler, 1998: Observations of the finescale structure of a dryline during VORTEX 95. *Mon. Wea. Rev.,* **126,** 525–550.

Charba, J., 1974: Application of gravity current model to analysis of squall-line gust front. *Mon. Wea. Rev.,* **102,** 140–156.

Cohn, S. A., and W. M. Angevine, 2000: Boundary layer height and entrainment zone thickness measured by lidars and wind-profiling radars. *J. Appl. Meteor.,* **39,** 1233–1247.

Cotton, W. R., and G. J. Tripoli, 1978: Cumulus convection in shear flow—Three-dimensional numerical experiments. *J. Atmos. Sci.,* **35,** 1503–1521.

Droegemeier, K. K., and R. B. Wilhelmson, 1987: Numerical simulation of thunderstorm outflow dynamics. Part I: Outflow sensitivity experiments and turbulence dynamics. *J. Atmos. Sci.,* **44,** 1180–1210.

Geerts, B., R. Damiani, and S. Haimov, 2006: Finescale vertical structure of a cold front as revealed by an airborne Doppler radar. *Mon. Wea. Rev.*, **234,** 251–271.

Grimsdell, A. W., and W. M. Angevine, 1998: Convective boundary layer height measurement with wind profilers and comparison to cloud base. *J. Atmos. Oceanic Technol.,* **15,** 1331–1338.

——, and ——, 2002: Observations of the afternoon transition of the convective boundary layer. *J. Appl. Meteor.,* **41,** 3–11.

Güldner, J., and D. Spänkuch, 2001: Remote sensing of the thermodynamic state of the atmospheric boundary layer by ground-based microwave radiometry. *J. Atmos. Oceanic Technol.,* **18,** 925–933.

Hane, C. E., R. M. Rabin, T. M. Crawford, H. B. Bluestein, and M. E. Baldwin, 2002: A case study of severe storm development along a dryline within a synoptically active environment. Part II: Multiple boundaries and convective initiation. *Mon. Wea. Rev.,* **130,** 900–920.

Hogg, D. C., F. O. Guiraud, J. B. Snider, M. T. Decker, and E. R. Westwater, 1983: A steerable dual-channel microwave radiometer for measurement of water vapor and liquid in the troposphere. *J. Appl. Meteor.,* **22,** 789–806.

Kingsmill, D. E., and N. A. Crook, 2003: An observational study of atmospheric bore formation from colliding density currents. *Mon. Wea. Rev.,* **131,** 2985–3002.

Martner, B. E., 1997: Vertical velocities in a thunderstorm gust front and outflow. *J. Appl. Meteor.,* **36,** 615–622.

May, P. T., 1999: Thermodynamic and vertical velocity structure of two gust fronts observed with a wind profiler/RASS during MCTEX. *Mon. Wea. Rev.,* **127,** 1796–1807.

Murphey, H. V., R. M. Wakimoto, C. Flamant, and D. E. Kingsmill, 2006: Dryline on 19 June 2002 during IHOP. Part I: Airborne Doppler and LEANDRE II analyses of the thin line structure and convective initiation. *Mon. Wea. Rev.*, **134,** 406–430.

Neiman, P. J., F. M. Ralph, R. L. Weber, T. Uttal, L. B. Nance, and D. H. Levinson, 2001: Observations of nonclassical frontal propagation and frontally forced gravity waves adjacent to steep topography. *Mon. Wea. Rev.,* **129,** 2633–2659.

Parsons, D. B., M. A. Shapiro, R. M. Hardesty, R. J. Zamora, and J. M. Intrieri, 1991: The finescale structure of a west Texas dryline. *Mon. Wea. Rev.,* **119,** 1242–1258.

Ralph, F. M., P. J. Neiman, and T. L. Keller, 1999: Deep-tropospheric gravity waves created by leeside cold fronts. *J. Atmos. Sci.,* **56,** 2986–3009.

Rasmussen, E. N., S. Richardson, J. M. Straka, P. M. Markowski, and D. O. Blanchard, 2000: The association of significant tornadoes with a baroclinic boundary on 2 June 1995. *Mon. Wea. Rev.,* **128,** 174–191.

Reuter, G. W., and M. K. Yau, 1987: Mixing mechanisms in cumulus congestus clouds. Part II: Numerical simulations. *J. Atmos. Sci.,* **44,** 798–827.

Rogers, R. R., W. L. Ecklund, D. A. Carter, K. S. Gage, and S. A. Ethier, 1993: Research applications of a boundary-layer wind profiler. *Bull. Amer. Meteor. Soc.,* **74,** 567–580.

Rotunno, R., J. B. Klemp, and M. L. Weisman, 1988: A theory for strong, long-lived squall lines. *J. Atmos. Sci.,* **45,** 463–485.

Schroeder, J. A., 1990: A comparison of temperature soundings obtained from simultaneous radiometrics, radio-acoustic, and rawinsonde measurements. *J. Atmos. Oceanic Technol.,* **7,** 495–503.

Solheim, F., J. R. Godwin, E. R. Westwater, Y. Han, S. J. Keihm, K. Marsh, and R. Ware, 1998: Radiometric profiling of temperature, water vapor and cloud liquid water using various inversion methods. *Radio Sci.,* **33,** 393–404.

Wakimoto, R. M., 1982: The life cycle of thunderstorm gust fronts as viewed with Doppler radar and rawinsonde data. *Mon. Wea. Rev.,* **110,** 1060–1082.

——, H. V. Murphey, E. Browell, and S. V. Asmail, 2006: The "triple point" on 24 May 2002 during IHOP. Part I: Airborne Doppler and LASE analyses of the frontal boundaries and convective initiation. *Mon. Wea. Rev.,* in press.

Weckwerth, T. M., and D. B. Parsons, 2006: A review of convection initiation and motivation for IHOP_2002. *Mon. Wea. Rev.,* **134,** 5–22.

——, T. W. Horst, and J. W. Wilson, 1999: An observational study of the evolution of horizontal convective rolls. *Mon. Wea. Rev.,* **127,** 2160–2179.

——, and Coauthors, 2004: An overview of the International H_2O project (IHOP_2002) and some preliminary highlights. *Bull. Amer. Meteor. Soc.,* **85,** 253–277.

Weisman, L. M., and R. Rotunno, 2004: "A theory for strong long-lived squall lines" revisited. *J. Atmos. Sci.,* **61,** 361–382.

Weiss, C. C., and H. B. Bluestein, 2002: Airborne pseudo–dual Doppler analysis of a dryline–outflow boundary intersection. *Mon. Wea. Rev.,* **130,** 1207–1226.

White, A. B., C. W. Fairall, and D. W. Thomson, 1991: Radar observations of humidity variability in and above the marine

atmospheric boundary layer. *J. Atmos. Oceanic Technol.,* **8,** 639–658.

Wilson, J. W., and W. E. Schreiber, 1986: Initiation of convective storms at radar-observed boundary-layer convergence lines. *Mon. Wea. Rev.,* **114,** 2516–2536.

——, and D. L. Megenhardt, 1997: Thunderstorm initiation, organization, and lifetime associated with Florida boundary layer convergence lines. *Mon. Wea. Rev.,* **125,** 1507–1525.

——, T. M. Weckwerth, J. Vivekanandan, R. M. Wakimoto, and R. W. Russell, 1994: Boundary layer clear-air radar echoes: Origin of echoes and accuracy of derived winds. *J. Atmos. Oceanic Technol.,* **11,** 1184–1206.

Wurman, J., 2002: The multiple-vortex structure of a tornado. *Wea. Forecasting,* **17,** 473–505.

Ziegler, C. L., and C. E. Hane, 1993: An observational study of a dryline. *Mon. Wea. Rev.,* **121,** 1134–1151.

——, and E. N. Rasmussen, 1998: The initiation of moist convection at the dryline: Forecasting issues from a case study perspective. *Wea. Forecasting,* **13,** 1106–1131.

——, W. J. Martin, R. A. Pielke, and R. L. Walko, 1995: A modeling study of the dryline. *J. Atmos. Sci.,* **52,** 263–285.